基于 CT 和磁共振 T2 加权图像双模态分类模型的自发性脑出血后脑水肿在 CT 图像上的分割

陈明扬[1,2] 朱时才[3] 贾富仓[1,2] 李晓东[3] Ahmed Elazab[1,2] 胡庆茂[1,2]

[1](中国科学院深圳先进技术研究院医学图像与数字手术研究室 深圳 518055)
[2](中国科学院大学 北京 100049)
[3](山东省临沂市人民医院 临沂 276000)

摘 要 自发性脑出血后脑水肿在 CT 图像呈现的模糊边缘是 CT 图像上实现脑水肿自动分割的一个严峻挑战。在磁共振 T2 加权图像上，脑水肿的边界相对清晰。因此，文章提出利用 14 套同时拥有磁共振和 CT 图像的病例，将其磁共振 T2 加权图像的手动分割金标准通过配准映射到 CT 空间，结合 CT 图像信息通过对配准后的结果进行机器学习得到脑水肿体素分类器，并利用此分类器进行 CT 图像上的脑水肿分割。采用近邻采样策略，选择公共测度子空间进行特征选择，基于支持向量机方法利用穷举法得到分割精度最高的水肿分类器；通过 36 套临床脑出血的 CT 数据的验证，结果显示该方法的 Dice 系数达到 0.859±0.037，明显高于基于区域增长的方法(0.789±0.036，P<0.000 1)、半自动水平集方法(0.712±0.118，P<0.000 1)和基于阈值的方法(0.649±0.147，P<0.000 1)。与之对比，使用 CT 手动分割金标准得到的分类器分割精度 Dice 系数(0.686±0.136，P<0.000 1)明显小于基于 T2 金标准的分类器。试验结果显示磁共振 T2 加权图像上脑水肿的清晰边界在精确区分水肿与周围正常脑组织的时候可能提供更强的约束。文章提出的方法为脑出血患者的脑水肿量化、病理改变严重性的评估、以及治疗提供潜在的工具。

关键词 自发性脑出血；脑水肿分割；多模态分割；支持向量机；采样策略；CT
中图分类号 TP 391.4 **文献标志码** A

Segmentation of Cerebral Edema Around Intracranial Hemorrhage on CT Scans Through Classification Model Learned from Patients with both CT and T2-Weighted Magnetic Resonance Images

CHEN Mingyang[1,2] ZHU Shicai[3] JIA Fucang[1,2] LI Xiaodong[3] Ahmed Elazab[1,2] HU Qingmao[1,2]

[1](*Laboratory for Medical Imaging and Digital Surgery*, *Shenzhen Institutes of Advanced Technology*, *Chinese Academy of Sciences*, *Shenzhen* 518055, *China*)
[2](*University of Chinese Academy of Sciences*, *Beijing* 100049, *China*)
[3](*Linyi People's Hospital*, *Linyi* 276000, *China*)

收稿日期：2016-07-30 **修回日期**：2016-08-15
基金项目：国家 973 项目(2013CB733800、2013CB733803)；国家自然科学基金-广东省联合基金重点项目(U1201257)；深圳市技术开发项目(CXZZ20140610151856719)；广东省创新团队项目(201001D0104648280)
作者简介：陈明扬，博士，研究方向为医学图像处理与模式识别；朱时才，硕士，研究方向为医学影像诊断；贾富仓，博士，研究方向为医学图像分析与手术导航；李晓东，博士，博士研究生导师，研究方向为神经工程学、神经康复治疗、以及神经机器接口；Ahmed Elazab，博士研究生，研究方向为医学图像处理；胡庆茂(通讯作者)，博士，博士研究生导师，研究方向为医学图像处理、模式识别和计算机辅助诊断，E-mail：qm.hu@siat.ac.cn。

Abstract Segmentation of cerebral edema from computed tomography (CT) scans for patients with intracranial hemorrhage (ICH) is challenging as edema does not show clear boundary on CT. By exploiting the clear boundary on T2-weighted magnetic resonance images, a method was proposed to segment edema on CT images through the model learned from 14 patients with both CT and T2-weighted images using ground truth edema from T2-weighted images to train and classify the features extracted on CT images. By constructing negative samples around the positive samples, employing the feature selection based on common subspace measures, and using support vector machine, the classification model was attained corresponding to the optimum segmentation accuracy. The method has been validated against 36 clinical head CT scans presenting ICH to yield a mean Dice coefficient of 0.859±0.037, which is significantly higher than that of region growing method (0.789±0.036, $P<0.000\ 1$), semi-automated level set method (0.712±0.118, $P<0.000\ 1$), and threshold based method (0.649±0.147, $P<0.000\ 1$). Comparative experiments have been carried out to find that the classifier purely from CT will yield a significantly lower Dice coefficient (0.686±0.136, $P<0.000\ 1$). The higher segmentation accuracy may suggest that clear boundaries of edema from T2-weighted images provide implicit constraints on CT images that could differentiate edema from its neighboring brain tissues more accurately. The proposed method could provide a potential tool to quantify edema, evaluate the severity of pathological changes, and guide therapy of patients with ICH.

Keywords intracranial hemorrhage; edema segmentation; multimodal segmentation; support vector machine; sampling strategy; computed tomography

1 Introduction

Intracranial hemorrhage (ICH) is one of the most common causes in adult acute neurologic injury, and it attracts much research attention for its high mortality and poor prognosis. It is a multi-factorial disorder with heterogeneous etiologies and may have potentially long-term debilitating outcomes[1-3]. Cerebral edema is an important secondary brain injury after ICH. Major factors contributing to the death in acute stage of spontaneous ICH caused by edema are intracranial hypertension and cerebral hernia[4]. Timely and effective diagnose and control of cerebral edema could help to reduce the mortality rate and prevent intracranial hypertension and cerebral hernia.

The mechanism of edema formation after ICH has not been fully understood[5]. Cerebral edema is present in most patients with ICH when imaged within 6 hours from onset, reaches the peak between 48 hours and 7 days, and is absorbed after 4 to 6 weeks[6]. Non-contrast computed tomography (CT) head scans remain the first choice for diagnosing ICH. However, on head CT scans, it is difficult to delineate edema regions due to substantial overlap of grayscale ranges between the edema and the neighboring cerebrospinal fluid (CSF) as well as white matter (WM), and unclear image boundaries. The major edema regions are low grayscale regions around hematoma within 1 centimeter radius[7].

Research on detection and quantification of cerebral edema after ICH from CT is relatively sparse. Bardera et al.[8] employed a semi-automated method based on level set to achieve a matching

ratio of 0.65. Volbers et al.[9] studied CT thresholds for edema to be 5-33 Hounsfield units using manually drawn hematoma from T2-weighted magnetic resonance (MR) images. Loncaric et al. employed a fuzzy expert system[10] and a hierarchical segmentation method[11] for edema segmentation. The last two studies did not report accuracy. We recently proposed to segment edema through region growing using advanced features such as local adaptive threshold and two dimensional entropy to yield an average Dice coefficient of 0.789[12]. The poor accuracy reflects the complexity and difficulty to segment edema from CT images.

T2-weighted MR imaging (MRI) has been proved to be beneficial to cerebral edema diagnosis in human stroke for decades, and has been the gold standard for accurate quantification of cerebral edema[13]. Unfortunately, application of MRI to assessing ICH is limited mainly due to its long imaging time (which is the main obstacle as ICH often needs urgent treatment), high cost and less availability than CT. Currently, CT is still preferred for assessing ICH patients due to its short imaging time, high sensitivity to hematoma, wide availability, and lower cost even though it could not show clear boundary of edema after ICH. It is thus of critical importance to enhance the delineation accuracy of edema from CT images.

This study is motivated by a postulation that the delineation accuracy of edema on CT images may be enhanced by adding additional constraints on the CT candidate edema regions through modeling features from patients with both CT and T2-weighted images. Support vector machine (SVM) is a widely used supervised learning method due to its good generalization capability from a few training samples[14-17], which will be employed for learning the classification model.

In this study, we propose to segment edema on CT images using model learned from 14 patients with both CT and T2-weighted images. The 14 ground-truths of cerebral edema on T2-weighted images manually drawn by radiologists are cast into CT space through affine transformation to learn the classification model of edema on CT images. Sixty-three features are devised to represent features of the edema including grayscale features, texture features and edge features, which are decreased to 60 features after feature selection based on common subspace (CS) measure. The method is then validated against 36 clinical CT scans presenting ICH and compared with other scenarios of classifiers, region growing method[12], semi-automated level set method[8], and threshold based method[9].

The rest are organized as follow. In Section 2, the method and materials are presented. In Section 3, the experiment results are given and compared with other methods. Discussion and conclusion are presented at last.

2 Method and materials

Fifty patients from Linyi People's Hospital of China were recruited for this study. The study was approved by the Institutional Review Board of the hospital. All patients gave written consent and provided permission for scientific and educational purpose. The patients were diagnosed with ICH and imaged within 6 hours to 2 weeks (43 within acute stage (within 72 hours) and 7 within subacute stage (72 hours to 2 weeks)). Since most CT and MRI data are not simultaneously available due to the

restriction of medical ethics, only 14 patients who were not suitable for surgery or were reluctant to have surgery, were imaged first with CT followed by T2-weighted MRI scans with a time interval of less than 3 hours. For other patients, a non-enhanced head CT scan was performed. All the CT and T2-weighted images were axial and obtained parallel to the orbito-meatal line. The image spacing was 0.46 mm within axial slices, and the slice distance was 4.8 mm. The statistics of the patients were: age range [18, 87] with an average of 59 years, and 17 female and 33 male.

The 14 patients who had both CT and MRI scans were chosen for training, while the rest were used for testing. The manual segmentation was conducted by expert radiologists from Linyi People's Hospital. For each patient, three manual segmentations of hemorrhage and edema on CT/MRI scans were delineated respectively by three radiologists. The final ground truth edema was composed of those voxels that were judged as edema by at least 2 experts.

Fig. 1 shows the flowchart of the method which consists of three components:

(1)Preprocessing to derive the brain and hematoma, and to register the T2-weigthed images with corresponding CT images of the 14 patients to cast the ground truth edema from registered MRI to CT images;

(2)Training to learn the classification model by devising appropriate features, appropriate sampling, and optimizing parameters of SVM on CT images;

(3)Categorizing voxels as lesion (either hematoma or edema) or non-lesion according to the classification model followed by contextual processing to eventually derive the edema on CT images.

In the following subsections, details will be elaborated.

2.1 Preprocessing

On CT scans, the brain is extracted according to

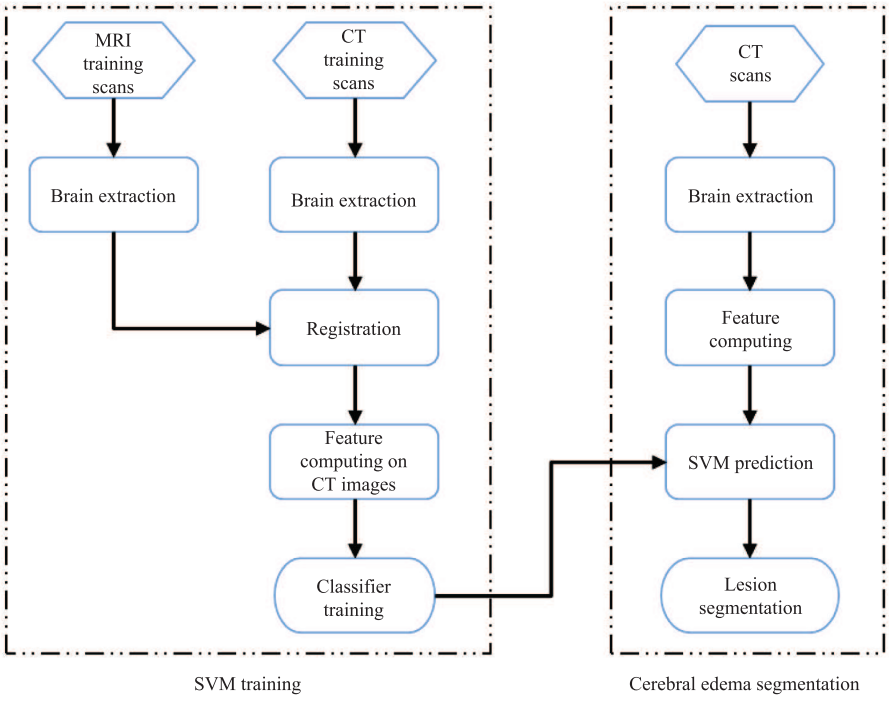

Fig. 1 Flow chart of the proposed method

Hu's report[18] based on fuzzy C-means clustering and connected component analysis. On T2-weighted images of the 14 patients, the brain is automatically delineated with an in-house software followed by expert refinement.

For each of the 14 patients with both CT and T2-weighted images, the two modalities should be registered to correct the difference in position, orientation and scale. The affine transformation of the 3D Slicer software is employed to register the T2-weighted images onto the CT space for each patient. Fig. 2 shows one axial slice after preprocessing.

2.2 SVM training

SVM training consists of feature computing, construction of training samples, parameter optimization of the classifier, and feature selection.

2.2.1 Feature computing

Grayscale information, texture information, and edge information in the form of histogram of oriented gradients (HOG)[19] are taken into account. The feature vector at a voxel consists of initially 63 quantities including 7 grayscale, 48 texture and 8 HOG quantities, which will be reduced to 60 quantities after feature selection.

2.2.1.1 Grayscale features

Inspired by the fact that human beings differentiate image regions according to their local contrast, we intend to incorporate the local contrast as one key grayscale feature. Due to the substantial grayscale overlap between edema and brain tissues, grayscale variability within a cerebral edema region and

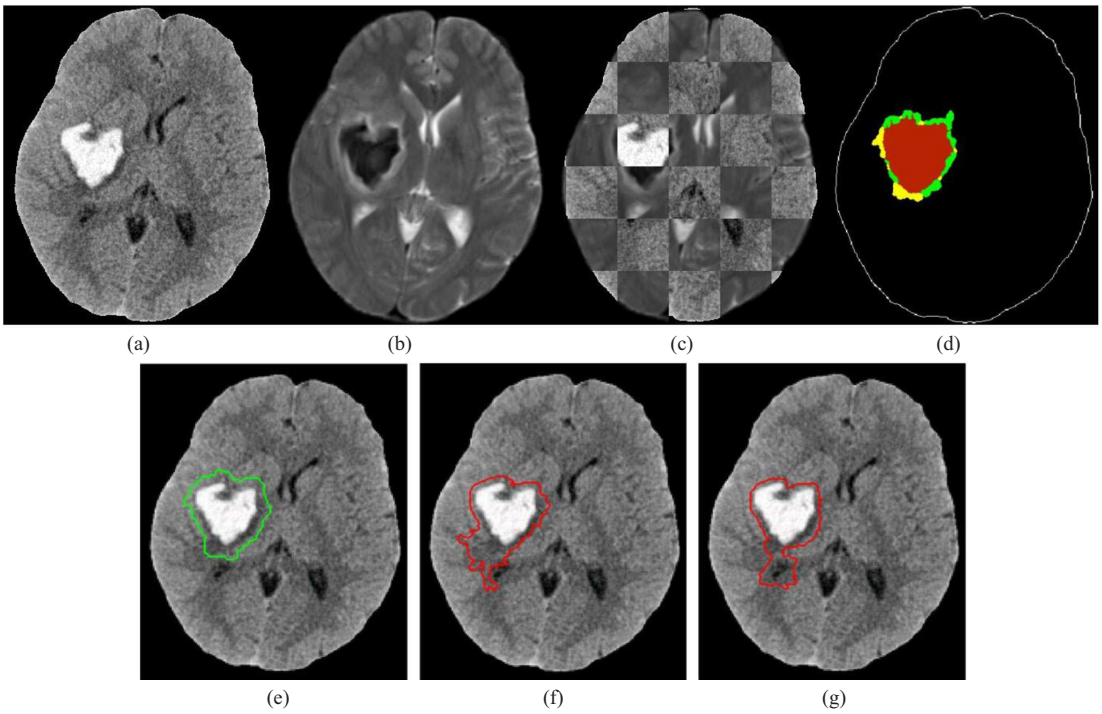

Fig. 2 Preprocessing: (a) a CT axial slice of the brain; (b) registered T2-weighted image corresponding to 2(a); (c) block unions of 2(a) and 2(b); (d) the ground-truth hematom+edema from 2(b) (dark red + green), and from 2(a)(dark red + yellow). For analyis purpose, (e), (f) and (g) are added to be respectively the ground truth edema from CT, segmented lesion from MR-GT classifier and CT-GT classifier (see texts in Section 4.3)

between edema of different patients, as well as the unpredictable size of edema, the window size of neighborhood for calculating the local contrast of edema voxels is non-trivial. We have studied the mechanism to change the window size adaptively for calculating local adaptive threshold based on local grayscale mean and standard deviation with adaptively variable window size[20].

The grayscale mean, median, and standard deviation within a neighborhood could represent its grayscale distribution. According to Padma's report[21], the size of neighborhood should generally be smaller than 7×7. Thus the grayscale distribution is calculated within 3×3 and 5×5 neighborhoods to be part of the feature vector.

2.2.1.2 Texture features

Here the gray level co-occurrence matrix (GLCM) is employed to describe the texture information relevant to lesion and non-lesion voxels on brain CT images. Following the convention, two voxels with a distance d and angle with respect to the x axis being θ, are involved for calculating the co-occurrence frequency $p(i, j, d, \theta)$, where i and j are respectively the grayscales of the starting and ending voxels. Four angles (0º, 45º, 90º, 135º) are used, with the d being respectively $(1,\sqrt{2},1,\sqrt{2})$ to calculate $p(i, j, d, \theta)$. For each angle, 12 texture features are calculated from $p(i, j, d, \theta)$ as below[22].

Angular second moment (ASM):

$f_1(d,\theta)=\sum_i\sum_j p(i,j,d,\theta)^2$

Contrast: $f_2(d,\theta)=\sum_i\sum_j (i-j)^2\, p(i,j,d,\theta)$

Correlation:

$$f_3(d,\theta)=\frac{\sum_i\sum_j (ij)^2\, p(i,j,d,\theta)-\mu_r(d,\theta)\mu_c(d,\theta)}{\sigma_r(d,\theta)\sigma_c(d,\theta)},$$

with $p_r(d,\theta)=\sum_i p(i,j,d,\theta)$, $p_c(d,\theta)=\sum_j p(i,j,d,\theta)$, $\mu_r(d,\theta)$, $\sigma_r(d,\theta)$, $\mu_c(d,\theta)$ and $\sigma_c(d,\theta)$ being respectively the means and standard deviations of $p_r(d,\theta)$ and $p_c(d,\theta)$.

Inverse difference moment:

$$f_4(d,\theta)=\sum_i\sum_j \frac{1}{1+(i-j)^2}\, p(i,j,d,\theta)$$

Sum average: $f_5(d,\theta)=\sum_k k p_{r+c}(k,d,\theta)$,

$p_{r+c}(k,d,\theta)=\sum_i\sum_{\substack{j\\ i+j=k}} p(i,j,d,\theta)$

Difference average: $f_6(d,\theta)=\sum_k k p_{r-c}(k,d,\theta)$,

$p_{r-c}(k,d,\theta)=\sum_i\sum_{\substack{j\\ |i-j|=k}} p(i,j,d,\theta)$

Variance: $f_7(d,\theta)=\sum_i\sum_j \left[i-\mu_i(d,\theta)\right]^2 p(i,j,d,\theta)$,

$\mu_i(d,\theta)=\sum_i\sum_j ip(i,j,d,\theta)$

Sum variance: $f_8(d,\theta)=\sum_i \left[i-f_5(d,\theta)\right]^2 p_{r+c}(i,d,\theta)$

Difference variance:

$f_9(d,\theta)=\sum_i \left[i-f_6(d,\theta)\right]^2 p_{r-c}(i,d,\theta)$

Entropy:

$f_{10}(d,\theta)=-\sum_i\sum_j p(i,j,d,\theta)\log\left[p(i,j,d,\theta)\right]$

Sum entropy:

$f_{11}(d,\theta)=-\sum_i p_{r+c}(i,d,\theta)\log\left[p_{r+c}(i,d,\theta)\right]$

Difference entropy:

$f_{12}(d,\theta)=-\sum_i p_{r-c}(i,d,\theta)\log\left[p_{r-c}(i,d,\theta)\right]$

2.2.1.3 HOG features

HOG captures the information related to shape such as edge or gradient, and HOG features are obtained as the histogram of local intensity gradient orientations $h(q)$ at each voxel q constructed from the intensity gradient magnitude $M(x, y)$ and orientation $\theta(x, y)$ (in the range of 0 to π) with a gradient operator such as Sobel operator[19].

The orientation of voxels (Dir) within voxel q's 5×5 neighborhood (Nq) are grouped into an orientation histogram with 8 bins, i.e., [0, π/8) (Dir_0), [π/8, π/4) (Dir_1), ⋯, and [7π/8, π] (Dir_7), weighted by the gradient magnitude of voxels within Nq. The gradient orientation histogram $\hat{h}_q\left(Dir_j\right)$ is thus

calculated as:

$$\hat{h}_q\left(Dir_j\right)=\sum_{\substack{\theta_i\in Dir_j\\ i\in N_q}} M_i(\theta_i) \tag{1}$$

where $j=0,1,2,\cdots,7$; θ_i and M_i are the gradient orientation and the gradient magnitude of voxel i.

The histogram $\hat{h}_q$ is normalized to form the final gradient orientation histogram:

$$h_q\left(Dir_j\right)=\frac{\hat{h}_q\left(Dir_j\right)}{\sum_{j=0}^{7}\hat{h}_q\left(Dir_j\right)+\xi} \tag{2}$$

where ξ is a constant (0.05) used to enhance the robustness to noise.

Each of the features $x^*_{i,j}$ is normalized into the range [−1,1] at each axial slice as follow:

$$x^*_{i,j}=\frac{2\times(x_{i,j}-m_j)}{M_j-m_j}-1 \tag{3}$$

where $x_{i,j}$ is the j^{th} feature at axial slice i; m_i and M_j are respectively the minimum and maximum value of the j^{th} feature at axial slice i, with $j=1,2,\cdots,63$. Indices of the original feature vector are given in Table 1.

2.2.2 Construction of training samples

Here the segmentation is converted to a binary classification, with foreground for lesion including hematoma and edema, and background for remaining brain tissues. Because the number of background voxels is much larger than that of the foreground, it is necessary to only sample representative background voxels to have a balanced number of training samples.

Edema appears as a region surrounding the hematoma with substantial grayscale overlap with the healthy brain tissues. Therefore, only voxels neighboring the lesion are sampled to represent the background. Specifically, at each axial slice with foreground voxels, morphological dilation is applied iteratively to the foreground with a disk structuring element of size 1 voxel until the size of the dilated foreground is 2.2 times the original foreground size. These background voxels included in the dilation process are then taken as the background to be sampled. Fig. 3 illustrates the distribution of these samples. Justification of the sampling strategy is addressed in Section 3.2.

2.2.3 SVM parameter optimization and classifier training

The main idea of SVM is to search for an optimal hyperplane that could best separate vectors from the two classes by mapping the vectors into a high-dimensional space[23].

For two-class classification problem, the training

Table 1 Indices of the original 63-dimenisonal feature vector

No.	Attribute
1	Local adaptive threshold
2-4	Grayscale mean, median, and standard deviation within 3×3 neighborhood
5-7	Grayscale mean, median, and standard deviation within 5×5 neighborhood
8-19	f_1-f_{12} with angle 0º
20-31	f_1-f_{12} with angle 45º
32-43	f_1-f_{12} with angle 90º
44-55	f_1-f_{12} with angle 135º
56-63	HOG features corresponding to edge orientations of [0, 22.5°), [22.5°, 45°), [45°, 67.5°), [67.5°, 90°) [90°, 112.5°), [112.5°, 135°), [135°, 157.5°), and [157.5°, 180°) respectively

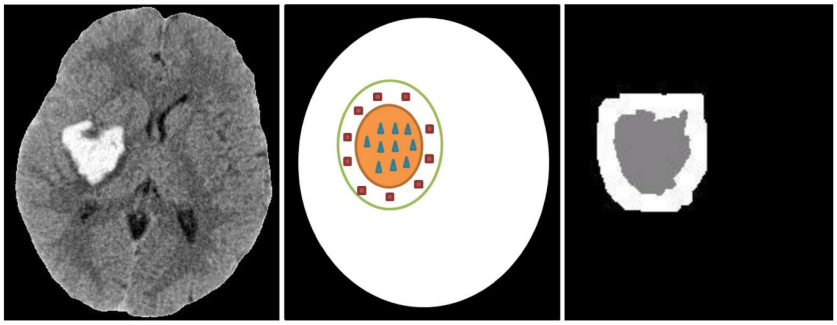

(a) (b) (c)

Fig. 3 Construction of training samples: (a) an original brain image; (b) the sketch map of sampling: all voxels of the foreground are taken as the postive sample (marked ▲) , while negative samples are chosen from neighboring voxels (marked ■ within the green circle); (c) samples of (a) according to (b) (gray for postive samples, and white for negative samples)

data x_i with label y_i are denoted as $\{x_i, y_j\}$, $i=1,2,\cdots,l$, $y_j \in \{-1,1\}$, $x_i \in \mathbf{R}^d$, where l is the number of training data and d is the dimension of feature vectors.

For nonlinearly separable samples, the objective function to be minimized is: $J(\boldsymbol{w})=\frac{1}{2}\|\boldsymbol{w}\|^2+C\sum_{i=1}^{l}\xi_i$, subject to $y_i(\boldsymbol{w}^{\mathrm{T}}x_i+b)-(1-\xi_i)\geqslant 0 \ \ \forall i$, where $\boldsymbol{w}$ is the weight matrix for the optimal hyperplane, $\boldsymbol{w}^{\mathrm{T}}$ is the transposed matrix of $\boldsymbol{w}$, the constant $C>0$ is a trade-off parameter between the maximization of the margin and minimization of the classification error. Researchers have suggested to apply kernel mapping for deriving the hyperplane with maximum-margin[24]. Three most widely used kernel functions are: linear kernel functions, polynomial kernel functions and radial basis functions with following equations[25]: linear kernel functions $K(x_i,x_j)=x_i^{\mathrm{T}}x_j$; polynomial kernel functions $K(x_i,x_j)=(\gamma x_i^{\mathrm{T}}x_{j+r})^d$, $\gamma>0$; and radial basis functions $K(x_i,x_j)=\exp\left(\gamma\|x_i-x_j\|^2\right)$, $\gamma>0$.

Appropriate selection of the kernel function is crucial for SVM training. To choose the appropriate kernel function, on the 14 data with both CT and T2-weighted images, we randomly take two-thirds of the training samples for training and the remaining one-third training samples for testing the accuracy of classification (the percentage of the correctly classified sample voxles) to find that the radial basis functions yield the best accuracy and are employed for subsequent training and classification (Table 2).

Table 2 The classification accuracy (%) of different types of kernel functions

Kernel function	Classification accuracy (%)
Linear	77.9
Polynomial	83.7
Radial basis	98.7

Penalty factor C and the parameter γ are two important parameters of the radial basis functions. We employ cross validation to optimize them using LIBSVM tool box[26]. With the SVM training parameters being optimized as $C=64$ and $\gamma=0.025$, positive samples as the CT voxels within the lesion region specified by the ground truth of registered T2-weighted images, negative samples as the CT voxels around the lesion detailed in Section 2.2.2, the classification model is attained using 14 data with both CT and T2-weighted scans.

2.2.4 Feature selection

To enhance classification accuracy and avoid

overfitting, feature selection is employed using CS measures[27]. The CS measure originates from the unique vector of each class, called common vector. The common vector is composed of the projection of the average feature vector of a class onto its own indifference subspace, which is spaned by eigenvectors to zero (or small) eigenvalues of the within-class covariance of each class. Specifically, the CS measure is computed as follow: 1) the average feature vector of one class is projected onto indifference subspace of other classes; 2) distances between the average feature of the projected class and the common vector of other classes are computed for each feature of the feature vector. The CS measure will yield a high value for the feature with high discriminative power and low value otherwise.

After the CS measure is obtained, features are sorted in descending discriminative power. After feature selection, 60 features are chosen for SVM training and classification. These 60 features include all the 63 features except the 3 features with feature indices of 58, 61, 62 according to Table A in Appendix, following the feature indices specified in Table 1. Justification of 60 features is elaborated in Section 3.1.

2.3 Cerebral edema segmentation

Cerebral edema is segmented in the following steps from CT images of patients with ICH. Firstly, preprocessing is carried out to derive the brain[18]. Then the hematoma is segmented based on local adaptive thresholds and case-based reasoning[20]. Thirdly, 60 features are calculated for brain voxels from axial slices with hematoma ($z=z_0$) or neighboring an axial slice with hematoma ($z=z_0-1$ and $z=z_0+1$), which are fed into the derived classification model from Section 2.2.3 to be classified as foreground or background (Fig. 4(b)). Fourthly, foreground regions with hematoma voxels are taken as lesion regions. As is known, a common problem for all classification based methods is holes within the foreground region to be filled. The last step is thus to fill the holes within lesion regions, subtract the hematoma voxels and take the rest as edema (Fig. 4(d)).

On an axial slice without hemorrhage but neighboring an axial slice with hemorrhage, if there are foreground regions from the classifier which overlap with lesion regions (having voxels with the same x and y coordinates) in the neighboring axial slice, these foreground regions are also taken as edema.

(a) (b) (c) (d)

Fig. 4 The procedure to segment the edema: (a) the original CT image; (b) foreground derived from the classifer; (c) the lesion after elimination of false foreground and filling holes, and (d) the segmented edema after hematoma is subtracted from the lesion

3 Results

The algorithm was implemented in Matlab version 2013a running on Microsoft windows with Core i5 3.2 GHz processor and 8 GB memory. The voxel-wise classification was applied to brain voxels with or neighboring hematoma. The average time consumption for one data was 11.83 minutes: 0.43 minutes in preprocessing, 9.47 minutes in feature calculation (mainly on calculation of the texture features), 1.62 minutes in SVM prediction, and 0.31 minutes in post processing.

To quantify the edema segmentation, the following measures are employed[28]: Dice coefficient, sensitivity, and specificity.

For comparison, two kinds of classifier are devised with the ground truth edema from MRI data and CT data, and are denoted as MRI-GT classifier and CT-GT classifier, respectively (GT for ground truth). Specifically, the MRI-GT classifier is trained using all 14 scans with both MRI and CT, while the CT-GT classifiers are designed using 36 CT scans from those patients without T2-weighted scans via leave-one-out cross validation. The classifiers can also vary in terms of number of classes: 2 classes and 3 classes. In the case of 2-classes classifiers, hematoma and edema are taken as the foreground while the remaining brain voxels are taken as the background. For 3-classes classifiers, hematoma, edema and remaining brain voxels are respectively taken as different classes. The proposed method is the MRI-GT classifier with 2 classes. To enable a fair comparison, the same procedure to eliminate the false foreground, fill holes within lesions and include pure edema regions without hematoma is also applied to all other classifiers.

The proposed method is also compared with the method to segment edema based on region growing[12], semi-automated level set method[8] and threshold based method[9].

3.1 Feature selection results

To devise a feature vector from the CS measure for 36 testing data, 4 patients (with ID 91833, 92035, 92142, and 92339) are chosen randomly for analysis. The experimental results for the feature selection of the 4 data can be found in Appendix.

Table 3 summarizes the dependency of the maximum classification accuracy and maximum Dice coefficient on the number of optimized features in terms of the CS measure. It can be seen that the

Table 3 Dependency of the segmentation performance on the number of features for the 4 randomly chosen CT data, numbers in the brackets are the numbers of features with the highest classification accuracy and Dice coefficient

Patient ID	Modality	Classification accuracy (%) (Feature dimension)		Dice coefficient (Feature dimension)	
		2-classes	3-classes	2-classes	3-classes
ID 91833	MRI-GT	95.843 (**60**)	90.766 (**35**)	0.890 (**60**)	0.686 (**35**)
	CT-GT	95.753 (**33**)	92.932 (**51**)	0.773 (**33**)	0.779 (**51**)
ID 92035	MRI-GT	95.377 (**60**)	91.630 (**35**)	0.922 (**60**)	0.859(**35**)
	CT-GT	95.088 (**33**)	91.702 (**51**)	0.912 (**33**)	0.891 (**51**)
ID 92142	MRI-GT	91.248 (**60**)	80.839 (**35**)	0.830 (**60**)	0.646 (**35**)
	CT-GT	88.022 (**33**)	84.588 (**51**)	0.815 (**33**)	0.724 (**51**)
ID 92339	MRI-GT	93.583 (**60**)	86.823 (**35**)	0.835 (**60**)	0.663 (**35**)
	CT-GT	93.277 (**33**)	89.075 (**51**)	0.789 (**33**)	0.696 (**51**)

proposed MRI-GT classifier with 2-classes yields the maximum classification accuracy and Dice coefficient. As the Dice coefficient for the 4 patients all reaches maximum at 60 features, eventually 60 features arranged in the descending order of the CS measure are chosen as the optimized features to form the feature vector. As the 3-classes classifiers yield substantially lower classification accuracy and Dice coefficient, further experiments will only be carried out for the 2-classes classifiers. Hence MRI-GT/CT-GT classifiers will mean the classifiers with 2-classes for brevity without confusion.

3.2 Different sampling strategies

A special training sample generation is employed as described in Section 2.2.2 in light of the postulation that brain voxels close to the edema are more relevant and difficult to be classified. To justify, two classifiers are designed: one using uniform sampling of negative samples to yield a significantly lower Dice coefficient (0.801±0.052, $P=0.009$), and the other using the combination of dilated voxels (1.5 times the original foreground size) and uniform sampling of the rest of the brain voxels (0.7 times the original foreground size) as the negative samples to yield a significantly lower Dice coefficient (0.810±0.039, $P=0.023$) for the 4 patient data. We also carry out experiments to see the accuracy dependency on the size of the negative samples using the 4 patient data with background size being from 1 to 1.8 times the original lesion size and a step 0.1. It is found that the proposed method yields the maximum classification accuracy and Dice coefficient when the foreground size is 1.2 times the lesion size.

Due to the higher Dice coefficient, the special sampling strategy detailed in Section 2.2.2 is adopted for all the experiments.

3.3 Performance evaluation

From Table A in the Appendix, it can be found that MRI-GT and CT-GT classifiers yield maximum classification accuracy and Dice coefficient with feature dimension of 60 and 33, respectively. Thus, we employ the MRI-GT/CT-GT classifiers with feature dimension of 60/33 on all 36 testing data for quantification, evaluation and comparison.

Two axial slices with acute and subacute ICH are shown respectively in Fig. 5 and 6, where the lesions delineated by experts are shown within the green contours while the lesions segmented by different methods are shown within the red contours. The Dice coefficients of the MRI-GT/CT-GT classifiers, region-growing method[12], semi-automated level set method[8], and threshold based method[9] for Fig. 5 are respectively 0.947/0.869, 0.805, 0.819 and 0.736; while the Dice coefficients for Fig. 6 are respectively 0.931/0.868, 0.904, 0.897 and 0.900.

Table 4 summarizes the classification accuracy, Dice coefficient, sensitivity, and specificity of the proposed method.

3.4 Comparison with the other classifier and existing methods

Performances of the classifiers, region growing method[12], semi-automated level set method[8], and threshold based method[9], are tested against the 36 testing data (Table 5). Note that the quantitative measures of the proposed method are shown in bold. Student's paired *t*-tests have been carried out to find that the proposed method yields significantly higher Dice coefficient than the CT-GT classifier, region growing method[12], semi-automated level set method[8], and threshold based method[9] (all $P<0.000\ 1$). As for sensitivity, the proposed

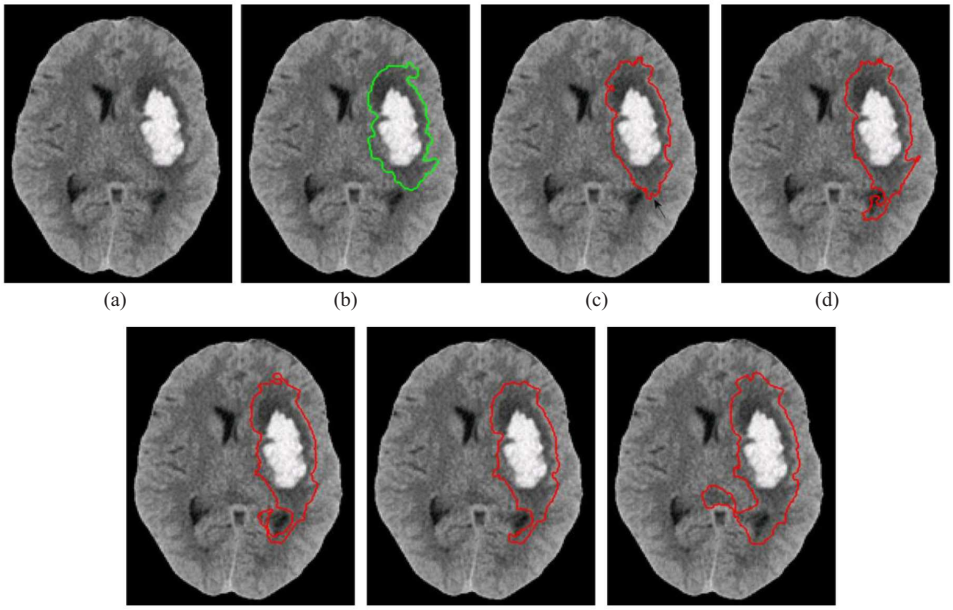

Fig. 5 Segmentation of edema with acute ICH: (a) a CT axial slice; (b) ground truth lesion within the green contour; (c) lesion segmented by the MRI-GT classifier; (d) lesion segmented by the CT-GT classifier; (e) lesion segmented by the region-growing method[12]; (f) lesion segmented by the semi-automated level set method[8]; and (g) lesion segmented by the threshold based method. Here black arrow (Fig. 5(c)) points to misclassified CSF

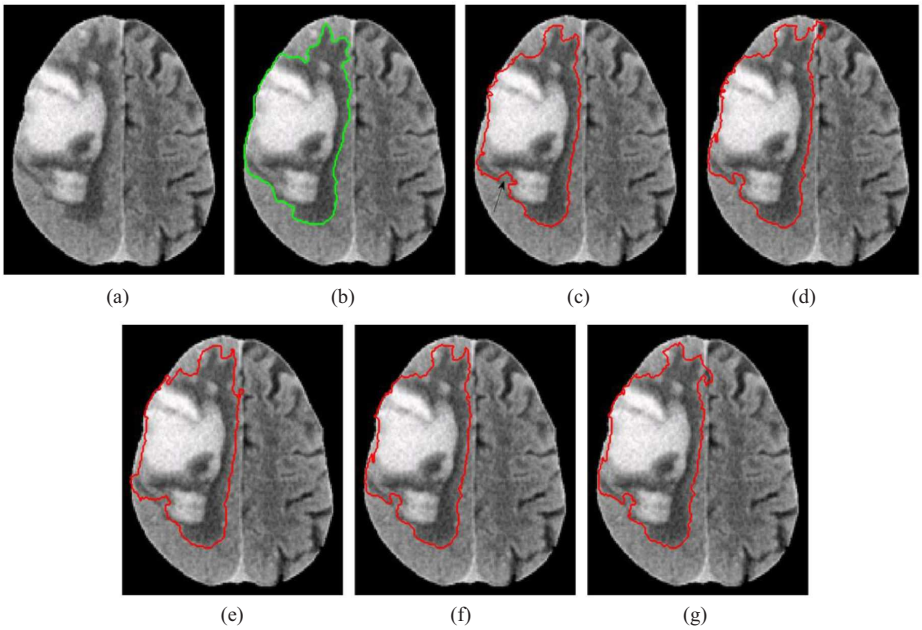

Fig. 6 Segmentation of edema with subacute ICH: (a) a CT axial slice; (b) ground truth lesion within the green contour; (c) lesion segmented by the MRI-GT classifier; (d) lesion segmented by the CT-GT classifier; (e) lesion segmented by the region-growing method [12]; (f) lesion segmented by the semi-automated level set method[8]; and (g) lesion segmented by the threshold based method. Here the black arrow (Fig. 6(c)) points to misclassified WM

Table 4 Quantification of the proposed method

Clinical stages	Classification accuracy (%)	Dice	Sensitivity	Specificity
Acute stage (29)	92.026±3.466	0.864±0.035	0.816±0.100	0.989±0.012
Subacute stage (7)	88.113±4.768	0.836±0.034	0.703±0.136	0.978±0.017
Total (36)	91.265±4.061 3	0.859±0.037	0.794±0.117	0.987±0.014

Table 5 Performance of the classifiers, region growing method[12], semi-automated level set method[8] and threshold based method[9]

Methods	Classification accuracy (%)	Dice	Sensitivity	Specificity
MRI-GT	**91.265±4.061 3**	**0.859±0.037**	**0.794±0.117**	**0.987±0.014**
CT-GT	86.299±6.228	0.686±0.136	0.653±0.206	0.966±0.043
Region growing[12]	—	0.789±0.036	0.823±0.054	0.972±0.012
Semi-automated level set[8]	—	0.712±0.118	0.744±0.136	0.979±0.035
Threshold based[9]	—	0.649±0.147	0.716±0.203	0.982±0.033

method performs significantly better than the CT-GT classifier ($P<0.000\ 1$) and the semi-automated level set method[8] ($P=0.046$); there is no significant difference between the proposed method and the region growing method[12] ($P=0.096$) as well as the threshold based method[9] ($P=0.247$). For the specificity, the proposed method is significantly better than the CT-GT classifier ($P=0.003$) and the region growing method ($P<0.001$); there is no significant difference between the proposed method and the semi-automated level set method[8] ($P=0.228$) as well as the threshold based method[9] ($P=0.392$).

4 Discussion

The main characteristics of the study are: to learn the classification model from two modalities (CT and MRI) so that the clear boundaries of edema on MRI could implicitly constrain the classification of edema on CT with unclear boundaries, to sort out the discriminative features based on the CS measure so that the combination of 60 features (the 63 features excluding features numbered 58, 61 and 62) are picked to achieve the best accuracy to differentiate lesion and non-lesion voxels with grayscale overlap on CT, and to segment the CT data with the classification model derived from a different group of patients.

A special sampling strategy to construct negative samples from around the positive samples is employed as described in Section 2.2.2 to achieve a Dice coefficient of 0.859±0.037. It was found that the classifier using homogeneous sampling of negative samples yielded a significantly lower Dice coefficient (0.760±0.082, $P<0.000\ 1$), and the classifier using the combination of dilated voxels (1.5 times the original foreground size) and uniform sampling of the rest of the brain voxels (0.7 times the original foreground size) as the negative samples to yield a significantly lower Dice coefficient (0.759±0.081, $P<0.000\ 1$). This additional experiment may suggest that negative samples around positive samples could yield better classification. Sampling strategy remains an open topic in pattern recognition and our sampling strategy may be employed for similar applications.

The proposed method yields significantly higher classification accuracy, Dice coefficient, sensitivity,

and specificity than the CT-GT classifier, region growing method[12], semi-automated level set method[8], and threshold based method[9] (all P $<$0.000 1) (Table 5).

4.1 Uncertainty of the ground truth edema on CT

It is non-trival to accurately delineate edema regions on CT scans with unclear image boundaries between the edema and CSF as well as WM due to substantial overlap of grayscale ranges[7]. To illustrate the inter-radiologist variability among three manual segmentations and the ground truth edema on CT and MRI, Dice coefficient and Hausdorff distance are calculated for one typical data (Table 6 and Fig. 7). It can be seen that 3 experts could delineate the edema with high constistency on MRI due to the clear boundaries of edema. On the other hand, there exist substantial differences among the 3 experts in delineating the edema boundary on CT due to unclear boundary, and different prior knowledge of radiologists employed. This uncertainty of edema boundaries is one major reason of the higher voxel misclassification on CT images.

4.2 Registration accuracy

The ground truth edema on MRI scans are cast onto the CT space for training the classifier model via affine transformation. Hausdorff distance and Dice coefficient are calculated to assess the registration accuracy and to quantify the diffierence between the manually segmented lesion boundaries on the CT and the MRI brain scans after registration. As listed in Table 7, the affine registration using 3D Slicer software yields an average Hausdorff distance of 1.629±0.192 mm and Dice coefficient of 0.989±0.0.004 based on the manually delineated hemorrhage for the same typical data shown in Fig. 7. On the contrary, the Hausdorff distance and Dice coefficient for the whole lesion are 0.839±0.035 and 8.922±2.022 mm, respectively. As is believed that hemorrhage could be well represented on both CT and T2-weighted images, the high Dice coefficient (0.989 vs. 0.839) and relative small Hausdorff distance (1.629 vs. 8.922) may imply that

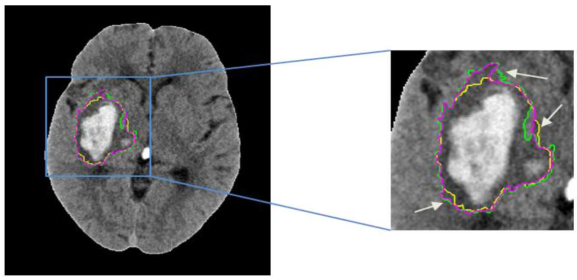

(a) CT scan

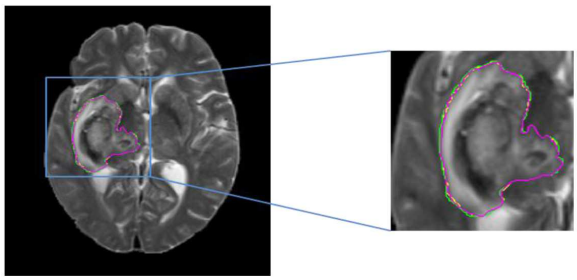

(b) MRI scan

Fig. 7 Differences among the manual delineations of 3 experts: the yellow, green, and purple contours respectively represent manual delineations by 3 experts

Table 6 Quantification of the manual delineations of 3 experts against the ground truth edema on CT and MRI of Fig. 7

Expert	CT scans		MRI scans	
	Dice	Hausdorff distance (mm)	Dice	Hausdorff distance (mm)
1	0.976±0.016	1.849±0.684	0.993±0.003	0.728±0.023
2	0.977±0.007	1.759±0.707	0.996±0.002	0.831±0.036
3	0.970±0.020	1.819±0.688	0.995±0.003	1.012±0.019

Table 7 Qauntification of registration using Dice coefficient and Hausdorff distance (mm)

Lesions	Dice		Hausdorff distance (mm)	
	Mean	Sd	Mean	Sd
Hemorrhage	0.989	0.004	1.629	0.192
Whole lesion	0.839	0.035	8.922	2.022

the registration is accurate to cast the desired lesion from MRI to CT space.

4.3 Differences between MRI-GT and CT-GT classifiers

Determination of the ground truth edema from CT scans for validation is a compromised choice due to the unavailability of ground truth edema from MRI for clinical practice. It is interesting to figure out the mechanism why the MRI-GT classifier could yield significantly higher Dice coefficient, sensitivity and specificity than the CT-GT classifier (Table 5).

Because the type of classifier and the way to select the features are the same, the difference in performance between MRI-GT and CT-GT classfiers is due to the difference in derivation of positive samples during training. In other words, the positive samples to train the classifiers determine the upper limit of the accuracy, or representation capability. It is thus reasonable to say that the positive samples to train the MRI-GT classifier (derived from the clear edema boundaries on MRI (Fig. 2(b)) is much better than the positive samples to train the CT-GT classifier (derived from the manual drawing of experts using complicated prior knowledge (Fig. 2(e)) to represent the charateristics of those 38 testing data in terms of Dice coefficient, sensitivity and specificity. To realize the representation capability, the rich information of lesion and non-lesion could best be encoded by 60 features of the MRI-GT classifier and 33 features of CT-GT classifier. We humbly believe that it is due to the better reprentation capability and the optimized features to implement the representation capability based on CS measures, the MRI-GT classifier is superior to the CT-GT classifier.

Take Fig. 2 for example, using the manually drawn edema on CT as quantification reference, the MRI-GT classifier yields a Dice coefficent of 0.844 (Fig. 2(f)) which is higher than that of the CT-GT classifier (Dice coefficient＝0.834, Fig. 2(g)). Alternatively, if we take the manually drawn edema on MRI as the quantitative reference, the MRI-GT classifier achieves an even higher Dice coefficient of 0.856 while the Dice coefficient of CT-GT classifier becomes even smaller (0.822).

4.4 Sensitivity to the ICH stage

From Table 4, it can be seen that the proposed method attains slightly higher Dice coefficient (P ＝0.321) for patients with acute ICH than that for patients with subacute ICH. It should be noted that at the subacute stage, the density of edema will increase while the density of hemorrhage will decrease with the absorption of edema and hemorrhage, resulting in an increased grayscale overlap between edema and WM as well as between hemorrhage and gray matter as compared with the ICH at the acute stage. These two factors may contribute to more edema misclassification for patients with subacute ICH. Even though that the MRI-GT classifier is trained from patients with acute ICH, it seems that the classifier has quite good generalization capability to be applicable to sub-acute stage ICH data.

4.5 Contributions

The main contributions are threefolds.

Firstly, the classification model for edema on CT has been built from patients with both MRI and CT scans. By doing so, the clear boundaries of edema from MRI provide implicit constraints on features in CT images that could differentiate voxels with similar grayscales into lesion and non-lesion voxels.

Secondly, a special sampling strategy has been employed to construct negative samples around the positive samples which could yield better classification accuracy than the uniform sampling of negative samples, as well as the negative samples derived from the combination of neighboring voxels and uniform sampling of the rest of brain voxels.

Thirdly, the CS measure is employed to find the optimum set of features to optimize the classification accuracy.

The proposed method could include non-edema voxels when they are neighboring edema and have similar grayscales to those of hematoma (arrow, Fig. 6(c)) and edema (arrow, Fig. 5(c)). On the other hand, the CT-GT classifier has a worse capability to differentiate edema from WM and CSF, in the form of including more CSF and WM as edema (Figs. 5 and 6). These observations are true for all the tested data. We may thus conclude that the added information from T2-weighted images for segmenting edema from CT images is to enhance the capability to differentiate edema from its neighboring WM and CSF.

4.6 Limitations

The proposed method will have large error when there are large neighboring non-edema regions with grayscales similar to those of edema (Fig. 8). For these cases, even experts may have difficulty differentiating edema from the rest. This problem is inherent to the inferior capability of CT in depicting edema. Possible solutions may be: imaging ICH with MRI, recruiting more subjects who have both CT and MRI scans to learn a more versatile model, and confining the range of edema around ICH (for instance, with few exceptions, one could assume that the edema will be within 1 centimeter of the ICH boundaries).

The proposed method is a straightforward way to incorporate the additional information from MRI into CT space for better delineating the ground truth

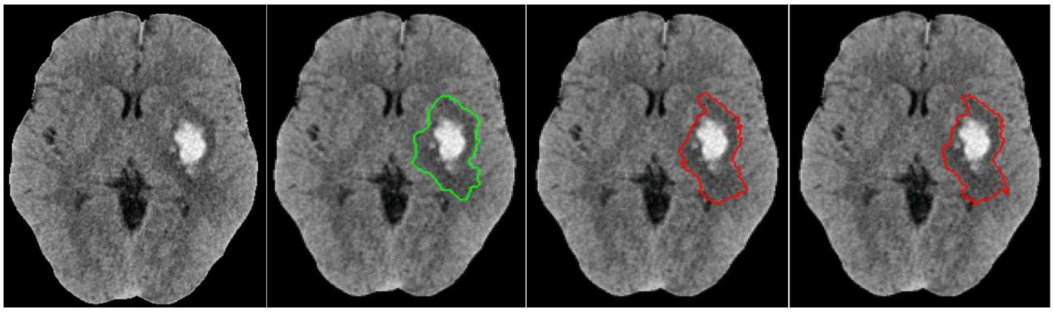

(a) (b) (c) (d)

Fig. 8 A case having scattered WM with similar grayscales to that of edema that is difficult for both the human being and the algorithm to delineate: (a) an original axial CT slice; (b) ground truth lesion within the green contour; (c) segmentation of the proposed method (Dice =0.781); and (d) segmentation of the CT-GT classifier (Dice=0.743), where the segmenetd lesion is the region within red contour

edema to train the classification model. In the future, we will explore an alternative way through transfer learning.

The proposed method adopts a traditional way for feature selection: extracting the possible relevant features followed by feature selection based on common subspace measure to pick out the discriminative features. In the future, we will explore an alternative way to pick out discriminative features through representation learning.

5 Conclusion

In conclusion, we have proposed a method to segment edema from CT images of ICH patients by constructing the classification model of lesion (edema plus hematoma) from 14 ICH patients with both CT and T2-weighted images, constructing negative samples around the positive samples, and optimizing features based on the CS measure. Validation on 36 clinical CT scans for patients with ICH shows that the proposed method could yield a mean Dice coefficient of 0.859±0.037 to be significantly higher than that of the classifier trained with CT ground truth lesion (0.686±0.136, $P<0.000\ 1$), region growing method[12] (0.789±0.036, $P<0.000\ 1$), semi-automated level set method[8] (0.712±0.118, $P<0.000\ 1$), and threshold based method[9] (0.649±0.147, $P<0.000\ 1$). The proposed method could provide a potential tool to quantify edema, evaluate the severity of pathological changes, and guide therapy of patients with ICH.

Acknowledgments

The authors would like to thank Dr. Xin Liu from Shenzhen Institutes of Advanced Technology for his valuable discussion on manually delineating the edema, 3 radiologists (Drs Guijin Du, Baotao Lv, and Qifei Xu) from Linyi People's Hospital for their efforts to draw the ground truth edema on both MRI and CT data.

References

[1] CaplanLR. Intracerebral haemorrhage [J]. Lancet, 1992, 339(8794): 656-658.

[2] Broderick JP, Brott T, Tomsick T, et al. Intracerebral hemorrhage more than twice as common as subarachnoid hemorrhage [J]. The Journal of Neurosurgery, 1993, 78(2): 188-191.

[3] Broderick JP, Adams HP, Barsan W, et al. Guidelines for the management of spontaneous intracerebral hemorrhage: a statement for healthcare professionals from a special writing group of the Stroke Council, American Heart Association [J]. Stroke, 1999, 30(4): 905-915.

[4] Broderick JP, Brott TG, Duldner JE, et al. Volume of intracerebral hemorrhage, a powerful and easy-to-use predictor of 30-day mortality [J]. Stroke, 1993, 24(7): 987-993.

[5] Xi G, Hua Y, Bhasin RR, et al. Mechanisms of edema formation after intracerebral hemorrhage: effects of extravasated red blood cells on blood flow and blood-brain barrier integrity [J]. Stroke, 2001, 32(12): 2932-2938.

[6] Wang DZ, Talkad AV. Treatment of intracerebral hemorrhage: what should we do now? [J]. Current Neurology & Neuroscience, 2009, 9(1): 13-18.

[7] Fainardi E, Borrelli M, Saletti A, et al. CT perfusion mapping of hemodynamic disturbances associated to acute spontaneous intracerebral hemorrhage [J]. Neuroradiology, 2008, 50(8): 729-740.

[8] Bardera A, Boada I, Feixas M, et al. Semi-automated method for brain hematoma and edema quantification using computed tomography [J]. Computerized Medical Imaging & Graphics, 2009,

33(4): 304-311.

[9] Volbers B, Staykov D, Wanger I, et al. Semi-automatic volumetric assessment of perihemorrhagic edema with computed tomography [J]. European Journal of Neurology, 2011, 18(11): 1323-1328.

[10] Loncaric S, Kovacevic D, Cosic D. Fuzzy expert system for edema segmentation [C] // The 9th Mediterranean Electrotechnical Conference, 1998: 1476-1479.

[11] Loncaric S, Cosic D, Dhawan AP. Hierarchical segmentation of CT head images [C] // Proceedings of the 18th Annual International Conference of the IEEE on Engineering in Medicine and Biology Society, 1996: 736-737.

[12] Chen MY, Hu QM, Liu ZC, et al. Segmentation of cerebral edema around spontaneous intracerebral hemorrhage [J]. Applied Mathematics & Information Sciences, 2013, 7(2): 567-570.

[13] Neumann-Haefelin T, Kastrup A, de Crespigny A, et al. Serial MRI after transient focal cerebral ischemia in rats: dynamics of tissue injury, blood-brain barrier damage, and edema formation [J]. Stroke, 2000, 31(8): 1965-1973.

[14] Way TW, Sahiner B, Chan HP, et al. Computer-aided diagnosis of pulmonary nodules on CT scans: improvement of classification performance with nodule surface features [J]. Medical Physics, 2009, 36(7): 3086-3098.

[15] Zhao X, Wong EK, Wang Y, et al. A support vector machine (SVM) for predicting preferred treatment position in radiotherapy of patients with breast cancer [J]. Medical Physics, 2010, 37(10): 5341-5350.

[16] Ozer S, Langer DL, Liu X, et al. Supervised and unsupervised methods for prostate cancer segmentation with multispectral MRI [J]. Medical Physics, 2010, 37(4): 1873-1883.

[17] Tan M, Deklerck R, Jansen B, et al. A novel computer-aided lung nodule detection system for CT images [J]. Medical Physics, 2011, 38(10): 5630-5645.

[18] Hu Q, Qian G, Aziz A, et al. Segmentation of brain from computed tomography head images [C] // Proceedings of the 27th Annual Conference of the IEEE on Engineering in Medicine and Biology Society, 2005: 3375-3378.

[19] Dalal N, Triggs B. Histograms of oriented gradients for human detection [C] // IEEE International Conference on Computer Vision & Pattern Recognition, 2013: 886-893.

[20] Zhang Y, Chen M, Hu Q, et al. Detection and quantification of intracerebral and intraventricular hemorrhage from computed tomography images with adaptive thresholding and case-based reasoning [J]. International Journal of Computer Assisted Radiology & Surgery, 2013, 8(6): 917-927.

[21] Padma A, Sukanesh R, Padma A, et al. Texture feature based analysis of segmenting soft tissues from brain CT images using BAM type artificial neural network [J]. Journal of Information Engineering & Applications, 2011, 1(4): 34-43.

[22] De Siqueira FR, Schwartz WR, Pedrini H. Multi-scale gray level co-occurrence matrices for texture description [J]. Neurocomputing, 2013, 120(10): 336-345.

[23] Cortes C, Vapnik V. Support-vector network [J]. Machine Learning, 1995, 20(3): 273-297.

[24] Boser BE, Guyon IM, Vapnik V. A training algorithm for optimal margin classifiers [C] // Proceedings of the 5th Annual Workshop on Computational Learning Theory, 1992: 144-152.

[25] Vapnik V. Statistical Learning Theory, 2nd Edition [M]. New York: Wiley, 1998.

[26] Chang CC, Lin C. LIBSVM: a library for support vector machines [J]. ACM Transactions on Intelligent Systems & Technology, 2011, 2(3): 389-396.

[27] Gunal S, Edizkan R. Subspace based feature selection for pattern recognition [J]. Information Sciences, 2008, 178(19): 3716-3726.

[28] Chang HH, Zhuang AH, Valentino DJ, et al. Performance measure characterization for evaluating neuroimage segmentation algorithms [J]. Neuroimage, 2009, 47(1): 122-135.

Appendix

The sorted lists of feature indices of 2-classes from the MRI-GT and CT-GT classifiers using CS measures are summarized in Table A. The SVM classifiers are trained using 2 features to 63 features according to the sorted lists (Table A) to find the optimum feature dimension with the highest Dice coefficient.

Table A Indices of features with descending discriminative power for the MRI-GT and CT-GT classifiers with 2 classes

MRI-GT	CT-GT
	ID 91833: 19, 18, 17, 16, 43, 13, 41, 15, 42, 12, 40, 14, 23, 20, 21, 22, 48, 51, 50, 49, 30, 31, 28, 29, 4, 1, 2, 34, 32, 33, 35, 7, 62, 46, 47, 44, 45, 6, 3, 55, 53, 52, 54, 37, 39, 38, 36, 59, 60, 63, 58, 9, 10, 11, 8, 56, 5, 61, 57, 24, 25, 26, 27
	ID 92035: 4, 2, 7, 12, 43, 13, 41, 14, 15, 40, 42, 5, 21, 20, 22, 23, 6, 1, 54, 52, 55, 53, 33, 34, 35, 32, 3, 36, 37, 38, 39, 16, 17, 18, 19, 28, 30, 31, 29, 61, 58, 63, 8, 9, 10, 11, 57, 44, 45, 47, 46, 51, 49, 48, 50, 59, 56, 62, 27, 25, 26, 24, 60
16, 19, 17, 18, 4, 2, 7, 5, 12, 14, 15, 42, 13, 40, 41, 43, 22, 23, 21, 20, 8, 9, 10, 11, 49, 50, 48, 51, 39, 36, 37, 38, 53, 55, 54, 52, 29, 31, 28, 30, 3, 35, 34, 33, 32, 45, 46, 44, 47, 1, 6, 26, 27, 24, 25, 60, 57, 63, 56, 59, 62, 61, 58	ID 92142: 4, 2, 7, 5, 41, 14, 42, 13, 40, 43, 15, 12, 22, 20, 21, 23, 1, 6, 32, 33, 34, 35, 39, 37, 36, 38, 3, 63, 54, 52, 55, 53, 16, 17, 19, 18, 61, 28, 30, 29, 31, 46, 44, 47, 45, 10, 11, 9, 8, 60, 56, 57, 62, 25, 27, 24, 26, 48, 49, 50, 51, 59, 58
	ID 92339: 16, 17, 18, 19, 4, 2, 22, 23, 21, 20, 12, 14, 41, 13, 15, 40, 42, 43, 31, 28, 29, 30, 48, 49, 51, 50, 1, 7, 32, 33, 35, 34, 53, 55, 52, 54, 6, 62, 3, 36, 38, 37, 39, 9, 8, 10, 11, 46, 44, 45, 47, 58, 5, 56, 59, 60, 63, 61, 57, 27, 24, 26, 25